Sensors and Actuators A 188 (2012) 181–189

Contents lists available at SciVerse ScienceDirect

Sensors and Actuators A: Physical

journal homepage: www.elsevier.com/locate/sna

# *In situ* wafer-level polarization of electret films in MEMS acoustic sensor arrays

M. Kranz [a,*], M.G. Allen [b], T. Hudson [c]

[a] 26184 Mooresville Road, Elkmont, AL 35620, United States
[b] Microelectronics Research Center, 791 Atlantic Drive, Georgia Institute of Technology, Atlanta, GA 30332, United States
[c] U.S. Army Aviation and Missile Research, Development and Engineering Center, RDMR-WSI, 7804 Patton Road, Redstone Arsenal, AL 35898, United States

ARTICLE INFO

*Article history:*
Available online 18 December 2011

*Keywords:*
Microplasma
Microcorona
Electret
Ultrasonic
Acoustic
Vibration

ABSTRACT

Polymer electrets, polymers with a quasi-permanent electrostatic polarization, are commonly employed in a macro-scale form factor within transducers such as the electret condenser microphone. In addition, MEMS-based electret transduction has been reported for both acoustic sensors and energy harvesters. In these micro-devices, the polymer film is typically polarized prior to assembly into the device. Common techniques employed in MEMS electret polarization include corona discharge and backlighted thyratron, with wafer-bonding and simple stacked assemblies being employed to perform the actual assembly and integration. In contrast, this paper reports a method for post-release *in situ* polarization of electret films within a MEMS device. The method utilizes microplasma discharges with self-aligned charging grids integrated within the device to charge fluoropolymer films in a fashion similar to the corona discharge technique. This *in situ* approach enables the integration of uncharged electret films into MEMS and subsequent post-fabrication charging, simultaneously enabling the formation of buried or encapsulated electrets as well as eliminating the need to restrict fabrication processes that might otherwise discharge pre-charged electret materials. The method is applied to a single-chip array of ultrasonic sensors designed to capture and analyze waveforms from impacts.



## 1. Introduction

### 1.1. Electret applications in MEMS

An electret, the electrostatic analog of a magnet, is a material with a quasi-permanent electrostatic polarization. Electrets can be fabricated from organic or inorganic materials, with polymers including Mylar® and Teflon® being commonly employed. Polarization of films can be accomplished through a number of mechanisms, with corona discharge [1] and backlighted thyratron [2] techniques being two common examples. Polymer electret films can be used directly as a sensor in a fashion similar to piezoelectric films [3,4], or indirectly as a voltage bias for sensors or power harvesters [5,6].

When used directly as a sensor element, changes to film geometry alter the film's electrostatic configuration. These changes can be amplified to provide usable signals in applications such as strain measurement, acceleration and vibration sensors, and acoustic detection. Although employed in a fashion similar to piezoelectric materials such as PZT, $BaTiO_3$, and $LiNbO_3$, polymer electrets offer advantages including MEMS-friendly process flows and options for conformal and transparent coating.

In addition, an electret can, through the large remnant voltage seen across its surface, be used as a permanent voltage bias within a sensor. This approach is used in the electret microphone, wherein the electret biases a movable diaphragm. Acoustic waves incident on the diaphragm move it with respect to the electret film, thereby creating a change in the electric field and a measurable output. Similarly, in energy harvesters, the electret film is often used to bias a mass that, when moved, leads to a current flow through an external circuit.

### 1.2. Electret integration challenges

In these applications, the use of electret films leads to challenges in overall device fabrication. In particular, the surface of the polymer must be exposed to the charging apparatus during the polarization process, thereby requiring the absence of fabricated structures above the film. Furthermore, once charged, significant discharge can occur if exposed to temperatures near the glass transition of the polymer, thereby limiting subsequent device fabrication to low-temperature processes.

As a result, most devices that employ active electret films are fabricated in two parts, one being a sensor component, and the other being a separate electret component. The electret can then be charged independently of the sensor fabrication. After completing fabrication of the two parts, they are assembled using a

* Corresponding author. Tel.: +1 256 714 8558.
*E-mail address:* michaelskranz@gmail.com (M. Kranz).

0924-4247/$ – see front matter © 2011 Elsevier B.V. All rights reserved.
doi:10.1016/j.sna.2011.11.039

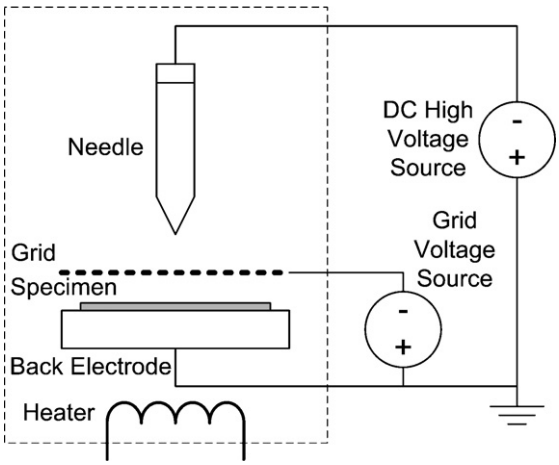


**Fig. 1.** A corona discharge is commonly employed to charge the exposed surface of a polymer electret yielding a quasi-permanent polarization. Charge uniformity is achieved through sample heating and a triode arrangement employing a charge grid separating the needle and the specimen.

low-temperature process. However, it is often desirable to fabricate the entire device on one wafer, and perform electret formation after wafer completion. *In situ* charging approaches can fulfill this goal.

## 2. Electret integration approach

Fig. 1 shows electret charging based on the corona discharge apparatus. A needle with a 2 mm diameter tip is suspended 10 mm above the specimen. A high voltage placed on the tip leads to ionization of the air near the tip. Charged species accelerate through a biased control grid towards the specimen, where they transfer charge to the surface. The large bulk resistivity of the polymer surface allows the charge to remain in place for long periods of time.

The *in situ* approach described here miniaturizes the traditional corona discharge apparatus, and embeds it within the sensor device itself, yielding microcorona discharges. Microcorona discharges have been previously achieved in microfabricated structures [7–9]. We demonstrate the use of this phenomenon for *in situ* charging of electrets and electret arrays. Fig. 2 shows a cross-section of an *in situ* charging grid comprising multiple micro corona electrodes. These electrodes are conceptually similar to the corona wires in copy machines and laser printers. They are suspended above the electret film using posts fabricated from the film itself. When energized, dielectric breakdown of the air in the gap leads to plasma discharges resulting in charge transfer to the electret film. This charging grid can be fabricated within the MEMS structure itself

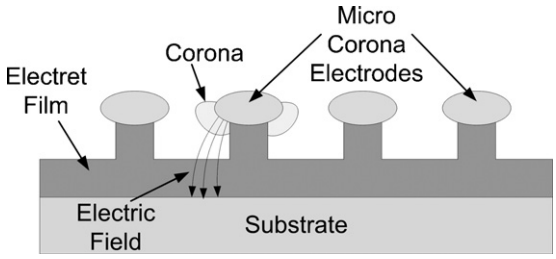


**Fig. 2.** Microfabricated electrode arrays suspended over the surface of the electret film through a working gas yield miniature microcorona sources. When energized by an external voltage, ionization at the edges of the electrodes, followed by charge migration to the film surface, yields film polarization.

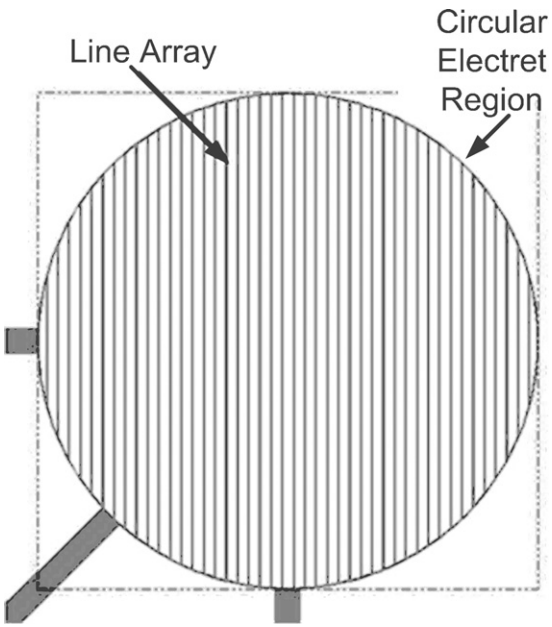


**Fig. 3.** An array of lines with consistent line widths and line spacings form a charging grid. This particular grid, when energized, yields a circular polarized area of the electret film.

and electret polarization can occur after complete device fabrication and release.

Fig. 3 shows a top view of the layout of a typical circular charging grid. This charging grid consists of an array of interconnected metallic lines with a uniform line width and spacing. After fabrication of the grid, the edges of the metal lines are suspended over the polymer film across a working gas. Upon energizing these metal lines, electrostatic discharges occur at the metal edges due to the high electric field strength at those edges.

## 3. *In situ* polarized sensor

The *in situ* polarization process employing the embedded charging grid was demonstrated in an ultrasonic sensor array designed to mechanically filter impact-generated acoustic and ultrasonic emissions propagating through a solid material, and convert those emissions into electrical signals. This sensor array included multiple high-Q transducer elements with differing natural frequencies that all fell within the band of frequencies generated by the impact, and could therefore be used as a high-Q filter array to process the acoustic signal. This narrowband sensor operation therefore differs from traditional broadband acoustic emission sensors and microphones designed to capture the signal with high-fidelity.

### 3.1. Sensor concept

Fig. 4 shows the impact scenario and the acoustic emission sensor under consideration. The sensor consists of a set of simple metal bridges suspended above microcorona charging grids and a polymer electret film. Once polarized, the electret film creates a voltage bias that capacitively couples with the suspended metal bridge. As the impact-generated stress pulse reaches the sensor, the anchors of the micro bridge experience a small displacement, leading to excitation of the bridge. As the bridge experiences motion relative to the electret film, a displacement current is generated in an external circuit. The frequency spectra of the impact-generated stress pulses under consideration fall within the range of 10–100 kHz. High-frequency resonances are thus desired, while low frequency sensor response represents a source of error. In addition, to

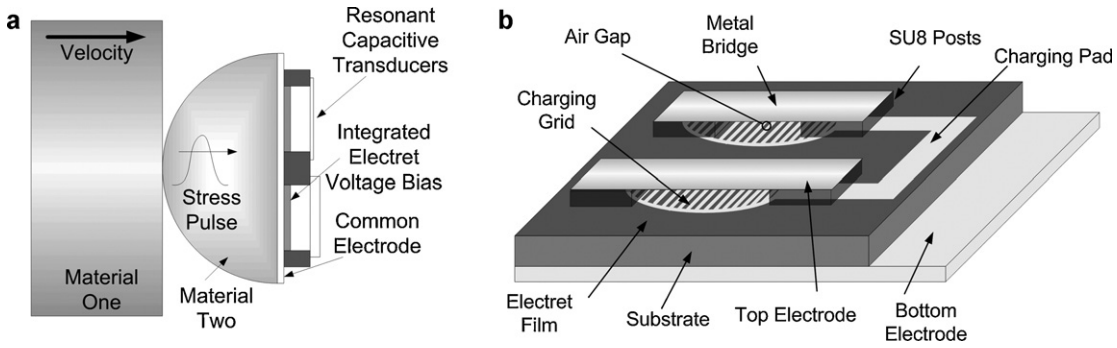


**Fig. 4.** (a) Multiple acoustic emission sensor elements attached to a structure capture stress pulses propagating through material two after impact with material one. Pulse width and height depend on the properties of materials one and two. Sensor elements with differing natural frequencies allow pulse characterization. (b) An *in situ* polarized electret-biased MEMS acoustic emission sensor includes top and bottom electrodes, a suspended metal bridge, an air gap, and an embedded microcorona charging grid with an electrode that allows placement of the high voltage source. Energizing the charging grid yields air gap ionization and subsequent polarization of the polymer film.

adequately separate the resonant frequencies within the array, high quality factors were desired. Therefore, micro bridges with sufficient venting and a large air gap were desired to minimize squeeze-film damping.

### 3.2. Sensor design

To align with the spectra of impact stress pulses, the natural frequencies for the individual transducers in the array were selected to cover a range from 10 kHz to 100 kHz. A single chip contained seven individual transducer elements, with each sensor suspended above its own charged electret area. The largest structure was 2 mm × 2 mm. Each subsequent structure was reduced in size by 200 μm. The natural frequency for a clamped–clamped bridge, neglecting effects of squeeze-film and other damping sources, residual film stress, and other dynamic effects, is given by

$$f = \frac{22.37 \times t}{2\pi L^2}\sqrt{\frac{E}{12\rho}} \quad (1)$$

where $t$ is the thickness of the structure, $L$ is its length, $E$ is the elastic modulus of the material, and $\rho$ is the density of the material. The nickel used in these structures was intended to be 10 μm thick, had a density of 8900 kg/m$^3$ and had an elastic modulus of 221 GPa. Table 1 lists the calculated natural frequencies for the expected lowest oscillation modes for each device in the array. Fig. 5 shows the layout of a full sensor chip consisting of these multiple bridges, with lengths varying from 800 μm to 2 mm, suspended over interconnected charging grids.

### 3.3. Sensor fabrication

CYTOP [10], a thermoplastic fluoropolymer encapsulant for electronics, is used as the polymer dielectric, and hence electret, in this sensor device because it can be spin-cast, has a high resistivity, and is easily etched in oxygen plasma. The microcorona charging grid structure is critical to the *in situ* charging method. It consists of multiple thin-film metal edges suspended a short distance above the polymer film. When energized by a high voltage, the sharp metal edges lead to high electric fields that ionize the air in the gap and force electric charge onto the polymer surface. In this work, the grid consisted of an array of narrow lines, approximately 5 μm wide, and separated by an approximately 40 μm gap. The metal lines are suspended approximately 2 μm above the polymer film through the simple fabrication process shown in Fig. 6. The metal is first deposited directly on the polymer, patterned, and then "suspended" by isotropically etching the polymer out from underneath it.

After fabrication of the charging grid, additional microfabrication steps, as shown in Fig. 7, are performed to build the acoustic sensor array [11]. SU8 is first spin-coated over the charging grids and a pattern of posts is exposed. The SU8 is not immediately developed, but instead undergoes a 12 h post-exposure bake. After the bake, the wafer is coated with Cr using a low-power e-beam evaporator. The low-power deposition minimizes SU8 crosslinking during the deposition. Following Cr deposition, a layer of gold is deposited. A photoresist plating mold is then spin-coated and patterned, followed nickel electroplating. Finally, the photoresist mold and the undeveloped SU8 are removed using a series of acetone and developer baths, yielding a fully released structure.

**Table 1**
The natural frequencies for the clamped-clamped beams in the MEMS transducer array were selected to cover the range from 10 kHz to 100 kHz.

| Length (mm) | Resonant frequency (kHz) |
|---|---|
| 2.0 | 12.812 |
| 1.8 | 15.817 |
| 1.6 | 20.018 |
| 1.4 | 26.146 |
| 1.2 | 35.558 |
| 1.0 | 51.247 |
| 0.8 | 80.074 |

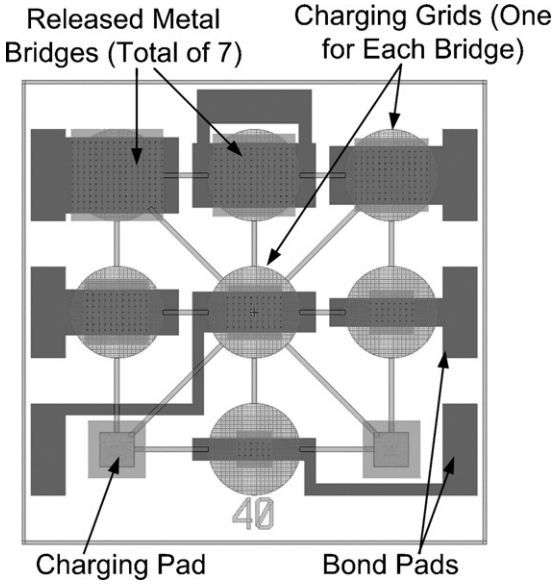


**Fig. 5.** To demonstrate simultaneous polarization of multiple electret sites, an entire array of sensors is fabricated with interconnected embedded microcorona charging grids. Each sensor in the array has a metal bridge with a different natural frequency.

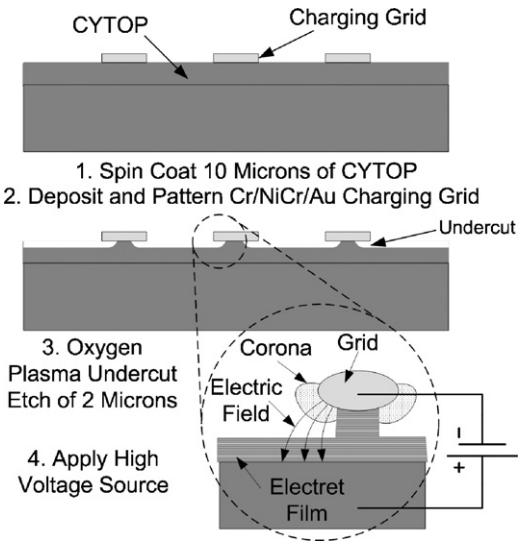


**Fig. 6.** The fabrication process for the "suspended" charging grid yields self-aligned structures and a small self-aligned air gap. The small air gap allows microcorona formation at lower voltages than typically required in a traditional corona discharge apparatus.

A SEM image of a final sensor device with a charging grid is shown in Fig. 8. The stress in the nickel film leads to curvature in the micro bridge and a shift in natural frequency from the previously calculated values. This shift must be accounted for during device operation. In addition, close-up images of the charging grid's metal edges show variations in the distance from the metal to the polymer, unevenness in the edge pattern itself, and sections of the edge that are folded over or bent. These imperfections lead to localized "hot spots" within the corona discharge, where discharge current is higher. The size scale of these variations is small compared to the overall size of the sensor electrodes, thereby limiting their impact on sensor operation. They do, however, limit the maximum polarization voltage that can be applied to the grid without yielding breakdown of the dielectric film.

## 4. *In situ* charging

### 4.1. Modeling

To predict the electric field within the air gap between the metal edge of the charging grid and the surface of the polymer film, an electrostatic finite element analysis was performed. Fig. 9 shows the electric field within both the gap and the polymer when

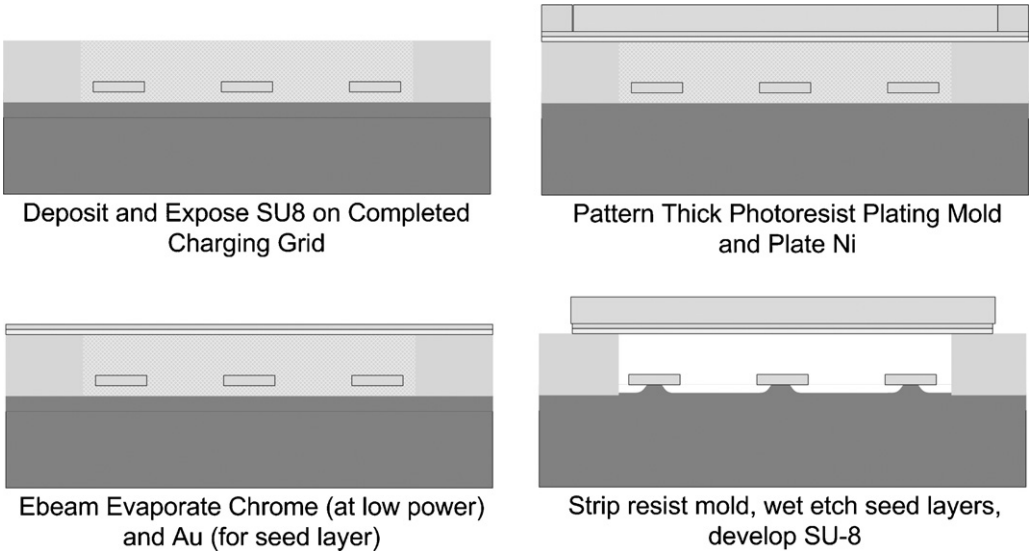


**Fig. 7.** The full sensor fabrication process builds the micromechanical sensor element above the unpolarized polymer electret film. All of the fabrication steps, including structure release, are performed prior to *in situ* polarization of the film.

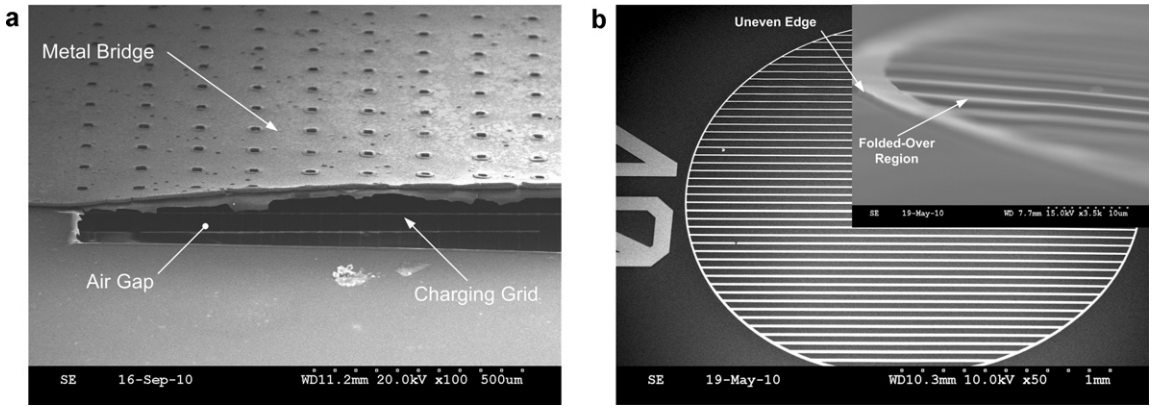


**Fig. 8.** (a) An SEM image shows a close-up view of a fabricated charging grid underneath the suspended metal bridge. Imperfections in the release process for the SU8 material led to film residue on the structure. (b) An SEM image of a completed charging grid. Close-up image shows defects in the metal edge that would lead to localized "hot-spots" in the corona discharge.

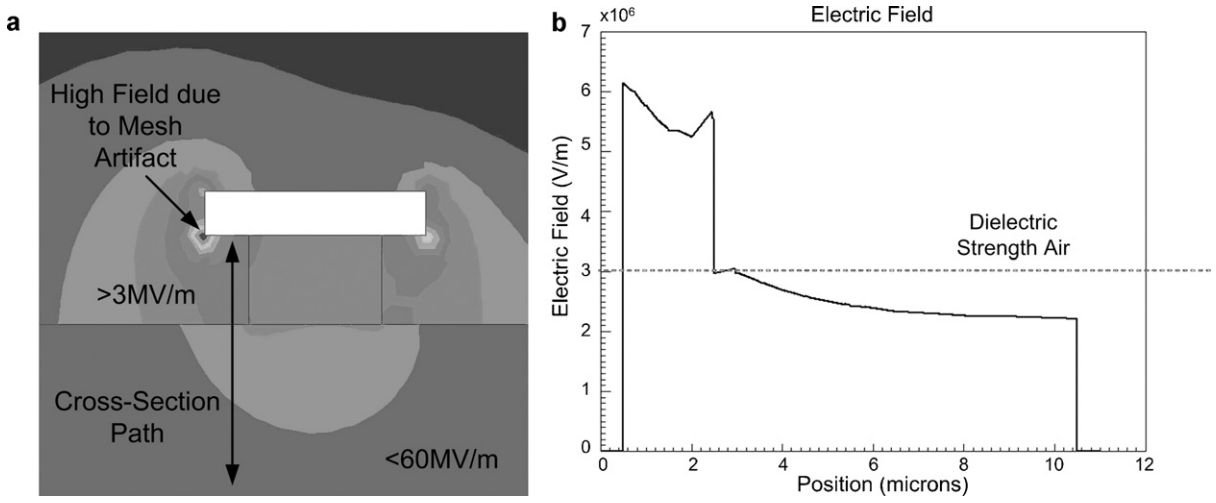


**Fig. 9.** (a) The small dimensions within the charging grid structure yields a high electric field strength greater than the dielectric breakdown of air at a relatively low voltage of −30 V. (b) The electric field in the polymer film is less than its dielectric strength, allowing the grid to remain energized.

the charging grid is energized to −30 V with respect to the substrate voltage. Within the gap, the electric field is greater than the dielectric strength of the air, approximately 3 MV/m, leading to a discharge condition within the gap. The calculation also shows that the electric field within the polymer does not exceed its breakdown, approximately 60 MV/m, thereby ensuring that the polymer insulates the charging grid from the substrate during the discharge process. The actual sharpness of the metal edge determines the maximum electric field within the gap. The finite element calculation in Fig. 9 modeled an ideal square edge, leading to an extremely high electric field near the edge. An actual charging grid would not have as sharp an edge, incorporating both defects and irregularities. These issues will be modeled and characterized in future work.

Based on the finite element calculation, the anticipated electric field strength lies within the Townsend regime [12] of electrostatic discharge. This regime (Fig. 10) is often utilized in systems such as avalanche detectors, radiation detectors, and other dark discharge processes. The applicability of the Townsend regime and the Townsend relation to small gap corona discharges is currently under investigation. However, the Townsend relation, an empirical relationship for the $I-V$ characteristics of the corona discharge, is employed in the equivalent circuit model of the *in situ* charging process, such that

$$I = AV(V - V_o) \tag{2}$$

where $I$ is the current through the discharge, $V$ is the voltage across the electrode gap, $V_o$ is the voltage corresponding to the onset of the corona, and $A$ is an empirical constant that takes into account items such as mean free path, collision probability, drift currents, and other complex phenomenon that occur in the discharge.

A SPICE model (Fig. 11) of the charging process was developed based on the discharge occurring in the Townsend regime. In the model, $V_1$ represents the high-voltage power supply that energizes the charging grid. $R_4$ is a large resistor that represents a leakage path and allows SPICE to derive a DC solution. $R_1$ was placed in the circuit to ensure that the voltage seen by an instrumentation

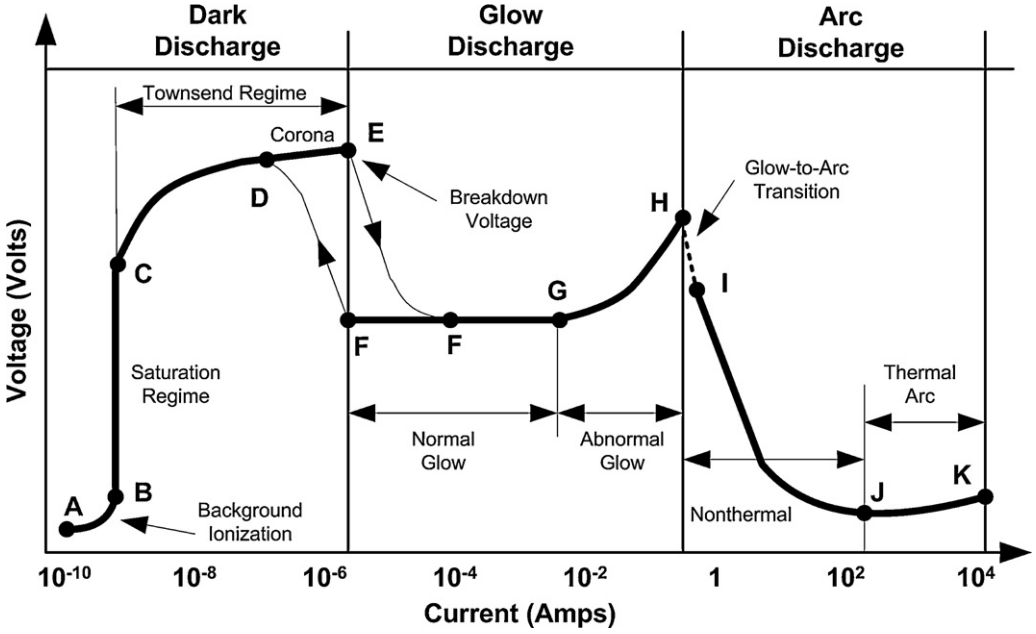


**Fig. 10.** The model for charging current in them microcorona charging grid is based on the Townsend regime including dark discharge and corona discharge.

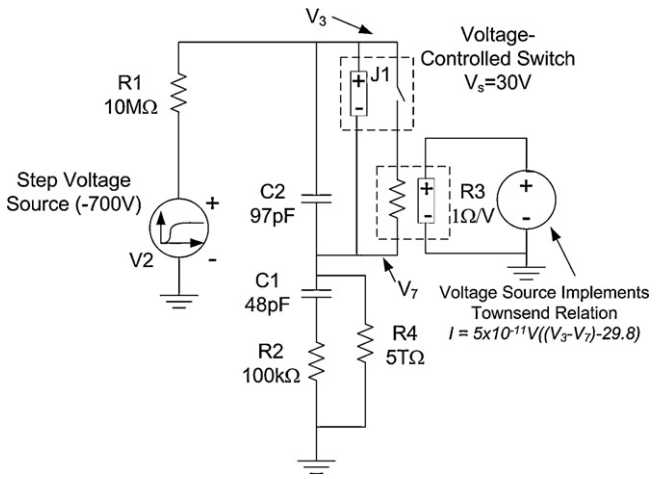


**Fig. 11.** SPICE model of the charging process.

amplifier, not shown in this figure, does not exceed rated maximums. $R_2$ is a current sensing resistor used to capture the current through the structure on an oscilloscope. $C_2$ represents the capacitance of the charging grid to the bottom electrode of the structure. $C_1$ represents the capacitance of the surface of the electret film to the bottom electrode. $R_3$ represents the "resistance" of the microplasma discharge. $J_1$ is a switch that accounts for the formation of the microplasma discharge only after a large enough electrostatic potential exists across the gap to result in dielectric breakdown of air.

To account for the nonlinearity of the corona discharge, $R_3$ is a voltage controlled resistor where the control voltage is calculated from the Townsend relation. A SPICE transient analysis was performed using this model. Fig. 12 shows the voltage across the sense resistor during the charging process. The two peak characteristic of the charging current is evident. The timing of the two peaks, as well as relative amplitudes, is highly dependent on the characteristics of the high voltage source used to energize the grid. For this simulation, an exponential voltage source with a rise time of 0.3 ms was utilized, approximating the turn-on time of the high voltage source used in actual charging experiments.

### 4.2. Process

In a finished device, and after the MEMS structure is released, the electret formation process is performed by energizing the grid to a high negative voltage (Fig. 13). When a suitable potential is achieved across the air gap between the grid and the polymer film

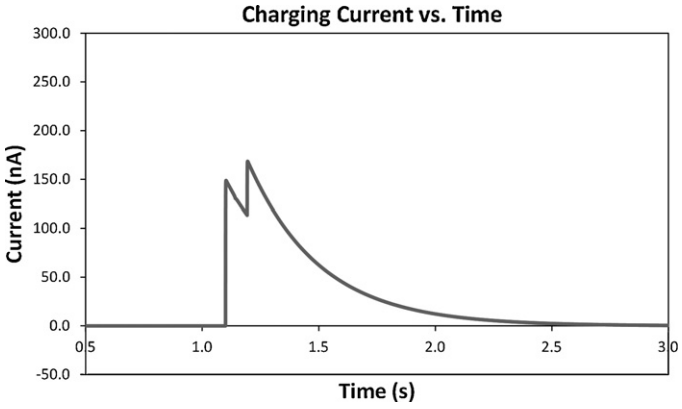


**Fig. 12.** Predicted discharge current using the SPICE model and Townsend regime approximation.

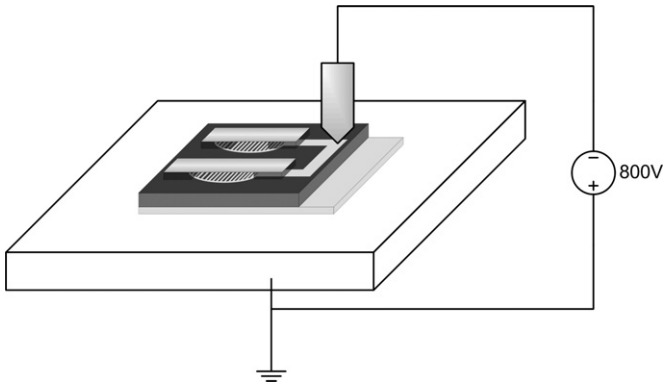


**Fig. 13.** After device fabrication, a probe placed onto the interconnect pad for the charging grids allows the grids to be energized, leading to electrostatic discharges and electret formation.

surface, a microcorona discharge occurs. Ions travel to the polymer surface where they transfer their charge. The charge builds up until sufficient potential is achieved such that the microcorona no longer exists. Fig. 14 shows the current through the grid structure during the charging cycle. The first peak represents charge being placed on the grid to raise its potential. The second peak represents the increase in current due to the onset of the microplasma discharge. The separation in time between the two peaks is due to the rise time of the voltage source, the output impedance of the voltage source, and the fact that the voltage source is current-limited, leading to differences from the SPICE model of the charging process. Actual charged sites achieved an electrostatic voltage of approximately −200 V after the first charging cycle when the grid was energized to −800 V.

Fig. 15 shows an optical image of the discharge event. The image on the left shows the charging grid as seen under normal lighting. The image on the right is of the same charging grid, but under no light conditions and captured during a portion of the discharge event. The intensity of the discharge is nonuniform across the charging grid and also time varying. This is due to nonuniformity of the metal edge sharpness, the orientation of the edge with respect to the polymer surface, and the actual gap between the edge and the

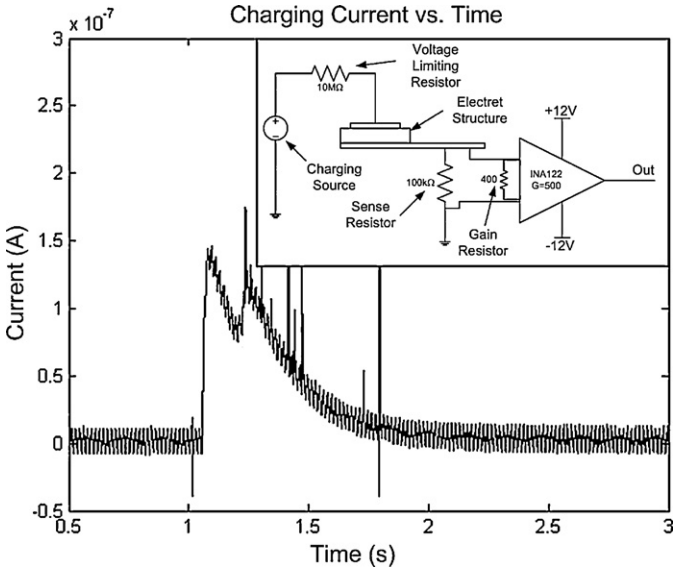


**Fig. 14.** A picoammeter circuit was used to measure the current flowing through the structure during the first charging cycle. This current demonstrated a second peak representing the turn-on of the corona discharge. This second peak was not evident in subsequent charging cycles of a charged sample.

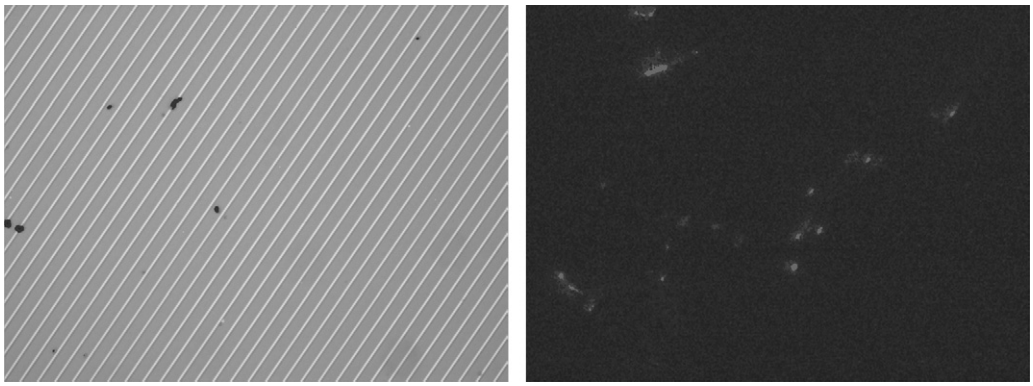

**Fig. 15.** An optical microscope image of the discharge process shows nonuniform discharge optical intensity. This intensity will depend on the strength of the electric field at the edges of the electrodes, a value that changes with time as the underlying polymer surface is charged.

polymer surface. These hot spots represent areas where discharge current is the highest and the charging rate is the highest. However, since the discharge event is voltage-limited, the variations in final voltage achieved are also limited.

### 4.3. Polarization results

A field-nulling vibrating reed electrometer was used after polarization to measure the remnant voltage of each charging site. Fig. 16 shows the achieved remnant voltage, after the application of −800 V to the charging grid, plotted against the line spacing of the grid. Large line spacings resulted in higher remnant voltages as seen by the electrostatic voltmeter. This is due to the masking of the charge by the area of the metal conductors. The highest measured voltage results from the highest density of metal edges with the smallest total grid surface area.

Fig. 17 shows the range of remnant voltages measured after polarizing multiple charging sites simultaneously on a single die. Each individual charging site is connected to the other charging sites and a contact pad. Upon application of the −800 V charging potential, all sites are charged simultaneously.

The variation in measured remnant voltages may be due to multiple factors. In particular, the polarization process can include "hot spots", areas where discharges are more intense and lead to larger surface charge densities. The probe of the electrometer used in these remnant voltage measurements is smaller than the electret area being measured. Therefore, these hot spots can interfere with the remnant voltage measurement. A higher resolution scan across the electret area would provide information about the uniformity of charge deposition. In addition, the metal of the charging grid that remains after polarization occurs can affect the remnant voltage measurement since its own stage of charge can interact with the bound charges, leading to a different electrostatic configuration and different remnant voltage measurement.

## 5. Sensor characterization

In the sensor array, a metal bridge transducer is suspended above each charging site; with each individual transducer in the array designed to exhibit a different natural frequency. This array was designed to perform spectral decomposition of an incident acoustic wave, with the natural frequencies spanning the range from 10 kHz to 100 kHz. When an impact or vibration is experienced, the output of the array represents a measurement of the spectrum of that input source. For this purpose, the natural frequency of the sensor element, as well as its sensitivity to the acoustic displacement, would be characterized.

Therefore, after fabrication and polarization, a sensor die was driven by a piezoelectric sheet in the test configuration shown in Fig. 18. The sensor die was coupled to the piezoelectric sheet using coupling oil, while the piezoelectric sheet was coupled to a Teflon® block. The piezoelectric sheet was driven by an external

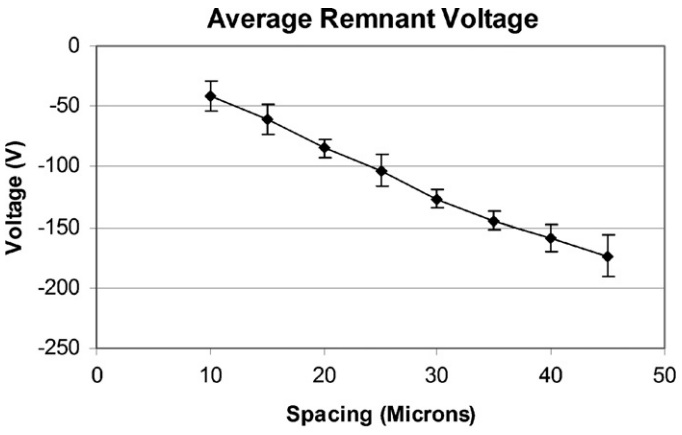


**Fig. 16.** The average remnant voltage achieved was dependent on the spacing between the microcorona electrodes. The remaining metal grid masks the voltage from structures above the grid, with the largest metal spacing yielding the last amount of masking.

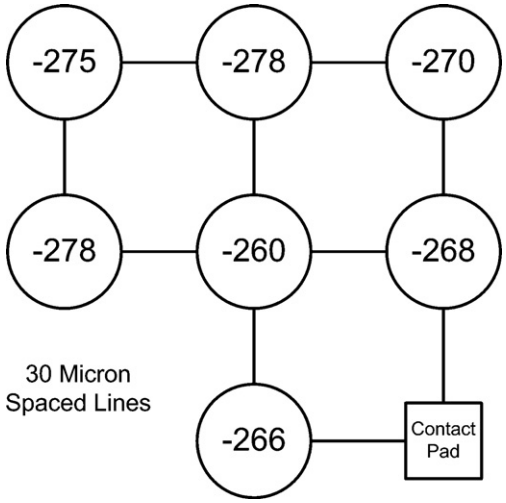


**Fig. 17.** The remnant voltage seen across multiple simultaneous charging sites shows a level of nonuniformity. Future process develops will focus on improving consistency of the charging method.

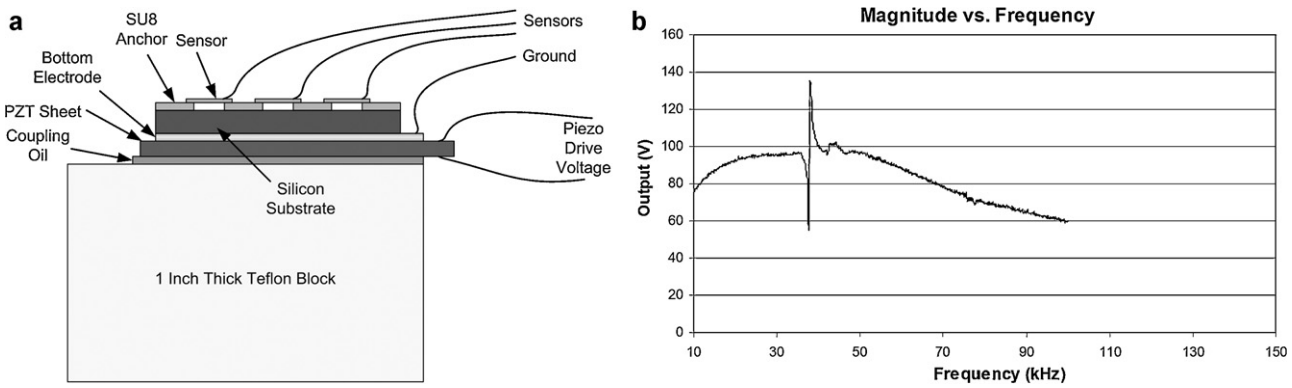


**Fig. 18.** (a) To characterize the frequency response of each element of the transducer array, a sensor die was coupled to a piezoelectric sheet, and a frequency sweep performed while capturing sensor element output. (b) A typical frequency response of the lowest frequency sensor in the array. This response showed a higher natural frequency than anticipated, likely due to micro bridge film curvature and stress.

function generator while the output from each individual sensor element was amplified and captured with an oscilloscope. The drive frequency of the piezoelectric sheet was scanned from 10 kHz to 100 kHz while the amplitude of the sensor output was recorded. Fig. 18 shows a representative scan of the sensor response for the lowest frequency device in the array. Each sensor element exhibited a higher natural frequency than as designed. As discussed earlier, this is likely due to the characteristics of the nickel film, including the curvature induced by the nickel stress. After characterization, some additional mass was added to the lowest frequency device to lower its natural frequency. Table 2 lists the final natural frequencies of each element in the array as determined through this characterization process.

After individual element characterization, the sensor array was incorporated into a drop tower impact system. Fig. 19 shows the sensor array attached to a hemispherical alumina structure and impacted by a projectile. Four projectiles with identical geometries, but made up of different materials, were dropped on to the hemisphere from a constant height. The materials used in the test were selected to provide a range of acoustic impedances, and included Teflon®, acrylic, stainless steel, and silicon nitride.

**Table 2**
The natural frequencies for the fabricated clamped-clamped beams in the MEMS transducer array were measured by sweeping frequency through the range from 10 kHz to 100 kHz.

| Length (mm) | Resonant frequency (kHz) |
|---|---|
| 2.0 | 37.8 |
| 1.8 | 42.2 |
| 1.6 | 49.4 |
| 1.4 | 56.2 |
| 1.2 | 73.3 |
| 1.0 | 92.1 |
| 0.8 | 118.4 |

Fig. 20 shows maximum peak voltage for each sensor from impacts between cylindrical projectiles of different materials and a ceramic hemisphere on which the sensor array is mounted. Hertzian contact theory [13] indicates that each material would present a unique signature across the frequency spectrum. This sensor array demonstrates the utility of *in situ* electret formation within the structures, and that multiple sites could be charged with the application of voltage to a single contact pad, allowing

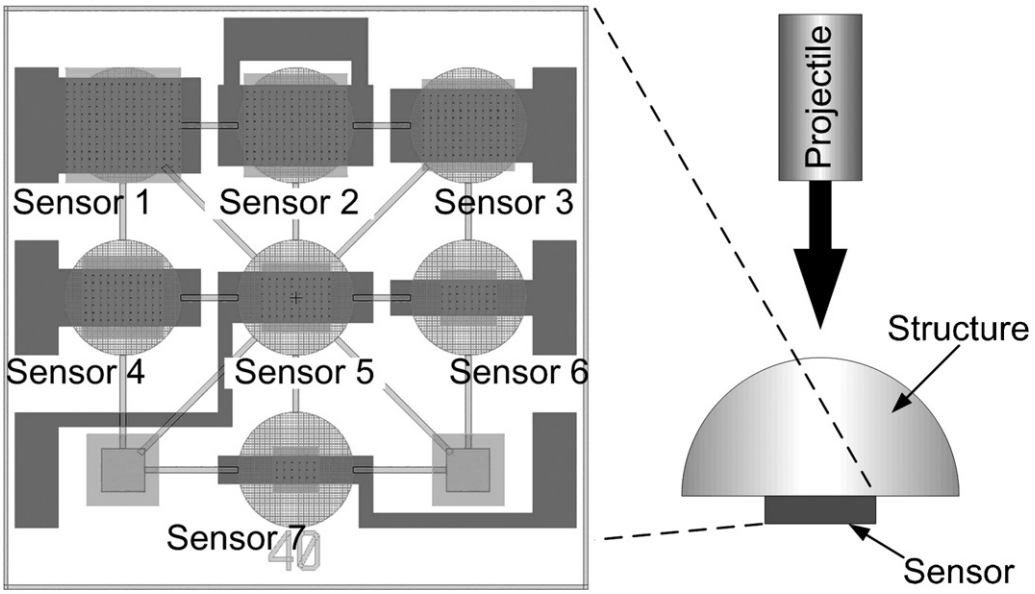


**Fig. 19.** The sensor array was assembled onto a hemispherical structure and placed in a ball drop impact setup. Impacts between the projectile and the structure yield acoustic waves in the structure that are detected by the sensors.

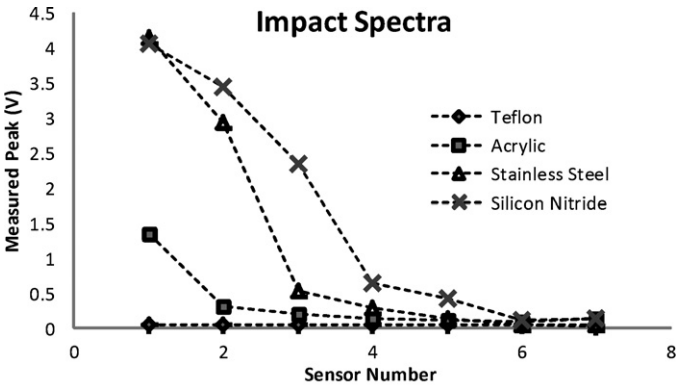


**Fig. 20.** Impacts with different materials excited the different transducers in the array to different levels, generating a "spectrum" of the impact. This array could be used to classify the materials involved in the impact through comparing the relative amplitudes of each sensor in the array.

the approach to be scaled to a full wafer implementation. This sensor array also demonstrated the ability to distinguish, through the use of multiple tuned sensor elements, between the acoustic signals generated during the impact of the structure with different materials.

## 6. Conclusions

*In situ* charging of electret areas within a MEMS device using microplasma discharges is presented in this paper. This electret integration approach is based on the formation of micro charging grids embedded within the MEMS structure during MEMS fabrication. After completing the fabrication flow and releasing the structure, energizing the embedded grid leads to electrostatic discharge from the metal edges of the grid to the electret film surface, leading to charge transfer and film polarization similar to the traditional macro-scale corona discharge process. In contrast, the *in situ* process can be performed after entire MEMS structure fabrication and release, thereby mitigating high-temperature process issues that electret films often experience. The process can also be scaled to the wafer-level, with multiple independent electret sites formed simultaneously within a device.

A variety of micro charging grids were fabricated and energized in order to validate and characterize charging grid design parameters, uniformity, and process models. Arrays of lines with varying line widths and spacings were fabricated to determine the effect of those parameters on subsequent remnant polarization of the electret. A masking effect was seen in these structures as the remaining metal of the charging grid masked the electret voltage from the electrometer used in device measurement. This is an artifact of the process and methodology that reduces overall electret performance even though surface charge density is higher than suggested. In addition, the nonuniformity of the discharge, with highest charge density being near the metal edges of the grid suggests alterations to grid geometry to optimize electret performance.

The *in situ* polarization process was incorporated into a MEMS ultrasonic sensor array device to demonstrate embedded electret fabrication. In the array device multiple sensor elements and multiple electret elements were fabricate in a wafer-level process, with electret formation occurring after device release. These sensor arrays demonstrate sensitivity to ultrasonic waves, as well as the separate of frequency components in the ultrasonic signals through the use of a range of natural frequencies within the array.

## Acknowledgements

The authors wish to thank Ms. Sharon Sanchez and Mr. Michael Allen for their microfabrication support, and in particular, their knowledge of SU8 processing, as well as Mr. Andy Jenkins for his support in modeling impacts and resonant structures.

## References

[1] Y. Arakawa, Y. Suzuki, N. Kasagi, Micro seismic power generator using electret power film, in: Power MEMS 2004, Kyoto, Japan, November 28, 2004.
[2] T.Y. Hsu, W. Hsieh, Y.C. Tai, A thin-film Teflon electret technology for microphone applications, in: Tech. Dig. Solid-State Sensors and Actuators Workshop, 1996.
[3] M. Goel, Electret sensors, filters and MEMS devices: new challenges in materials research, Current Science 85 (August (4)) (2003).
[4] T.H. Hsu, C.N. Yeh, Y. Su, Piezoelectric PDMS electrets for MEMS transducers, in: IEEE MEMS 2010, Hong Kong, January 25–28, 2010.
[5] T. Sterken, K. Baert, R. Puers, S. Borghs, Power extraction from ambient vibration, in: Proceedings of the Workshop on Semiconductor Sensors, Veldhoven, the Netherlands, November 29, 2002, pp. 680–683.
[6] E. Halvorsen, E.R. Westby, S. Husa, A. Vogl, N.P. Østbø, V. Leonov, T. Sterken, T. Kvisterøy, An electrostatic energy harvester with electret bias, in: Transducers 2009, Denver, CO, June 21–25, 2009.
[7] S. Lee, D. Kim, M.D. Bryant, F. Ling, A micro corona motor, Sensors and Actuators A 118 (2005) 226–232.
[8] C.G. Wilson, Y.B. Gianchandani, Silicon micromachining using *in situ* DC microplasmas, Journal of Microelectromechanical Systems 10 (March (1)) (2001).
[9] M. Honzumi, A. Ueno, K. Hagiwara, Y. Suzuki, Soft-X-ray-charged vertical electrets and its application to electrostatic transducers, in: 23rd IEEE International Conference on MEMS (MEMS 2010), Hong Kong, January, 2010.
[10] Y. Sakane, Y. Suzuki, N. Kasagi, The development of a high-performance perfluorinated polymer electret and its application to micro power generation, Journal of Micromechanics and Microengineering 18 (September) (2008) 104011, 6 pp.
[11] C. Chung, M. Allen, Uncrosslinked SU-8 as a sacrificial material, Journal of Micromechanics Microengineering 15 (1) (2005) N1–N5.
[12] R. Tirumala, Corona discharges in sub-millimeter electrode gaps, Journal of Electrostatics (2010).
[13] G. McLaskey, S. Glaser, Hertzian impact: experimental study of the force pulse and resulting stress waves, Journal of the Acoustical Society of America 128 (September) (2010) 1087–1096.

## Biographies

**Michael Kranz** earned a Bachelor of Science degree in Engineering Physics from Cornell University in 1996. Mr. Kranz then attended Carnegie Mellon University, where he earned a Master of Science degree in Electrical and Computer Engineering and performed research in micro-scale inertial sensors. After completing his graduate studies in 1998, Dr. Kranz moved to Redstone Arsenal to manage research at Morgan Research Corporation working in MEMS, nanotechnology, and fiber optics. In May 2011, Mr. Kranz earned a Ph.D. from the Georgia Institute of Technology. His thesis focused on nano-scale sensors and electro-active materials for the classification of acoustic waveforms.

**Mark Allen** received three bachelor degrees from the University of Pennsylvania in 1983: the B.A. in Chemistry, the B.S.E. in Chemical Engineering, and the B.S.E. in Electrical Engineering. He then attended the Massachusetts Institute of Technology, receiving the S.M. degree in Chemical Engineering and the Ph.D. degree in the field of microelectronics in 1986 and 1989, respectively. Dr. Allen serves as Executive Director, Institute for Electronics and Nanotechnology at Georgia Tech, and leads the Microsensor and Microactuator Group, where he has graduated over 27 Ph.D. students. He has published almost 90 refereed journal papers and 165 refereed conference papers.

**Tracy Hudson** earned Bachelor and Master's degrees in electrical engineering from the University of Alabama in Huntsville (1988, 1991) and a Ph.D. in engineering from The Pennsylvania State University (1997). He is a Senior MEMS Research Engineer with the U.S. Army's AMRDEC at Redstone Arsenal, AL. He has been recognized for his scientific achievements on numerous occasions to include the bestowal of the U.S. Army's Research and Development Award in 1991, 2003, and 2010. His current technical interests include microfabrication process development, MEMS device prototyping (inertial, microwave, acoustic sensors, piezoelectric materials, and power generation/management), and nanotechnology applications.